Available online at www.sciencedirect.com

ScienceDirect

journal homepage: www.elsevier.com/locate/he

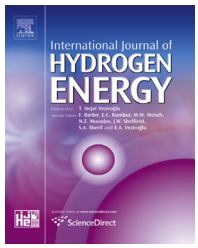

Three dimensional stress analysis of solid oxide fuel cell anode micro structure

Selahattin Celik [a,*], *Beycan Ibrahimoglu* [b], *Serkan Toros* [a], *Mahmut D. Mat* [c]

[a] *Nigde University, Mechanical Engineering Department, 51245 Nigde, Turkey*
[b] *Abdullah Gul University, Mechanical Engineering Department, 38039 Kayseri, Turkey*
[c] *Meliksah University, Mechanical Engineering Department, 38280 Kayseri, Turkey*

ARTICLE INFO

Article history:
Received 7 July 2014
Received in revised form
8 September 2014
Accepted 20 September 2014
Available online 11 October 2014

Keywords:
Solid oxide fuel cell
Micro level modeling
Stress analysis
Anode

ABSTRACT

One of the most common problems in solid oxide fuel cells (SOFCs) is the delamination and thus the degradation of electrode/electrolyte interface which occurs in the consequences of the stresses generated within the different layers of the cell. Nowadays, the modeling of this problem under certain conditions is one of the main issues for the researchers. The structural and thermo-physical properties of the cell materials (i.e. porosity, density, Young's modulus etc.) are usually assumed to be homogenous in the mathematical modeling of solid oxide fuel cells at macro-scale. However, during the real operation, the stresses created in the multiphase porous layers might be very different than those at macro-scale. Therefore, micro-level modeling is required for an accurate estimation of the real stresses and the performance of SOFCs. This study presents a microstructural characterization and a finite element analysis of the delamination and the degradation of porous solid oxide fuel cell anode and electrode/electrolyte interface under various operating temperatures, compressing forces and material compositions by using the synthetically generated microstructures. A multi physics computational package (COMSOL) is employed to calculate the Von Misses stresses in the anode microstructures. The maximum thermal stress in the electrode/electrolyte interface and three phase boundaries is found to exceed the yield strength at 900 °C while 800 °C is estimated as a critical temperature for the delamination and micro cracks due to thermal stress generated. The thermal stress decreases in the grain boundaries with increasing content of one of the phases (either Ni or YSZ) and the porosity of the electrode. A clamping load higher than 5 kg cm^{-2} is also found to exceed the shear stress limit.

Introduction

Solid oxide fuel cells (SOFCs) are considered as a promising candidate achieving the energy vision of the future in the view of the fuel flexibility, high conversion efficiency, low emission and cheap raw materials [1]. Many researches have focused to enhance the service life of SOFCs and to reduce the fabrication costs. One of the most essential weaknesses that needs to be

* *Corresponding author*. Tel.: +90 388 225 24 50; fax: +90 388 225 01 12.
E-mail address: scelik@nigde.edu.tr (S. Celik).
http://dx.doi.org/10.1016/j.ijhydene.2014.09.110

improved is the high operating temperature which leads to the delamination of the cell component and the degradation of the cell performance due to material issues. A typical SOFC comprises anode electrode, electrolyte and cathode electrode layers. Each of these layers consists of different materials. In addition to main functioning materials, a certain amount of electrolyte material is generally added to both electrodes in order to improve the cell performance by increasing the electrochemical reaction zones known as triple phase boundaries. All layers of a cell exhibit different elasticity modulus, Poison's ratio and the coefficient of thermal expansions (CTE). High temperature gradients created during the cell operation may result in micro/macro cracks in the cells because of mechanical property differences [2]. Specifically, the differences in CTE cause an additional stress in the electrode/electrolyte interfaces and the grains in the electrode structure. Mechanical constraints as a result of stack assembly and temperature gradient generated due to the continuous electrochemical reactions during the stack operation further complicate the stress distribution and the defect initiation. Some authors have reported on the residual stress at room temperature after redox [3]. However, detailed experimental measurements and analysis of the mechanical behavior under SOFC operation conditions have not yet been reported [4].

With the advent of 2D and 3D visualization techniques, there have been increasing number of studies on the investigation of the defect mechanisms in SOFCs at micro-scale. Although 2D microstructures are relatively easy to obtain using conventional techniques, 3D studies are exciting due to representing more realistic microstructures and providing deeper understanding of the defect mechanisms. Therefore, there is a remarkable increase in the number of the studies employing improved 3D imaging and the finite element analyses on 3D microstructures. Advanced focused ion beam (FIB)-scanning electron microscopy (SEM) [5–13] and X-ray computed tomography (XCT) [14,15] devices are generally utilized in order to obtain the representative volume element (RVE) used in the finite element simulations. 3D visualization techniques have been employed for both the anode and the cathode microstructures [10,11]. Clague et al. [16] investigated the microstructure of the anode electrode with FIB-SEM microscope in order to obtain the representative volume element for the numerical analysis of the stresses at Ni and YSZ interfaces. Gunda et al. [17] used 3D microstructural visualization technique for the LSM cathode again employing FIB-SEM and a digital filtering algorithm for better presentation of the microstructure. A CFD analysis was then performed for 3D microstructure. Similarly, Carraro et al. [18] used 3D cathode microstructure in the advanced CFD analysis. The distribution of the oxygen concentration in the cathode was analyzed. The study showed that the 3D microstructural representation provide a better analysis of degradation mechanism during the SOFC operation.

Although 3D or 2D microstructural images obtained by using advanced visualization devices are essential for a realistic analysis, synthetically generated microstructures also help the investigation of the complex multi physics involved in SOFC electrodes. Synthetic microstructures are relatively easy to generate and eliminate the expensive equipment for visualization of real 3D microstructures. Synthetic microstructures are also useful for analyzing the effects of the production and/or the operation parameters on the macroscopic mechanical or physical properties of SOFC electrodes. It is also possible to optimize desired mechanical and/or physical properties. Currently, new electrode structure development is based on the trial and error approach which is costly ineffective and time consuming. Thanks to advanced software which make possible to generate any kind of microstructure and analyze their effect on both performance and mechanical/physical properties. The microstructure generation software allows the investigation of the influences of the microstructure parameters like the particle size, the quantity and the morphology of the grains. Otherwise it is almost impossible to separate them experimentally [19].

In the present study, the synthetic microstructures are generated for the electrolyte supported Ni-YSZ cells by "Dream 3D" (Digital Representation Environment for Analyzing Microstructure in 3D) which is based on the statistical approach. In the software, it is possible to create variety of microstructures by adjusting percentage of constituting materials such as Ni, YSZ and porosity, as well as particle sizes. The generated microstructures are used for the determination of the interactions between Ni and YSZ phases, and the stress distributions and the delamination of the electrode/electrolyte interfaces at various operating temperatures. The effects of contact pressure on the delamination are also numerically investigated.

Microstructure generation in Dream 3D

Using the synthetically generated microstructures in the finite element software enables us to investigate the effects of the manufacturing and/or process parameters on the stress generation at the electrode/electrolyte interface leading to the delamination and the performance loss in SOFC. In this study, the effects of different amounts of Ni, YSZ and porosity in the anode structure are investigated. The effects of the operating temperature on the delamination are also studied. The package DREAM 3D (Digital Representation Environment for Analyzing Microstructure in 3D) [19–21] is used to generate synthetic microstructures of Ni-YSZ from the statistics gathered in the characterization phase. In the microstructure generation process, the grains were selected as the ellipsoid form and their sizes were determined by using the SEM analysis. The grain sizes of the phases were varied as between 0.5–2 μm and 1–3 μm for Ni and YSZ, respectively. The three-dimensional grain size distribution was estimated from these measurements and the distributions of grains were obtained by calibrating the parameters μ and σ values i.e. the average value and the standard deviation of the lognormal grain size distribution, respectively. For the YSZ phase, μ and σ values were selected as 0.8 and 0.1, respectively while those for Ni phase are 0.4 and 0.1, respectively. For the pores, on the other hand, these values were determined as 0.8 and 0.1, respectively [22]. Similarity of the synthetically generated microstructures is very satisfactory in the view of grain sizes and distributions of the phases as it can be seen in Fig. 1. The anode microstructure is generated in 50 × 50 × 50 voxel size

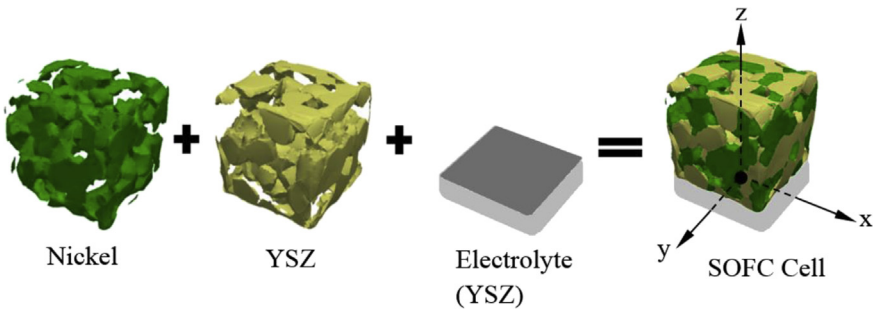

Fig. 1 – Synthetic micro structure build with Dream 3D software (Green: Nickel, Yellow: YSZ, Gray: Electrolyte). (For interpretation of the references to color in this figure legend, the reader is referred to the web version of this article.)

having 10 × 10 × 10 μm^3 volume. The electrolyte has 10 × 10 × 2 μm sizes and considered as fully dense. The size of computational domain is chosen based on FIB tomography analyses of similar studies in the literature [11,16].

A range of anode microstructures is obtained by arranging the amount of Ni/YSZ phases and porosity. A reference case with 35% Ni/30% YSZ/35% pore composition was chosen based on our previous experimental experience which was shown to

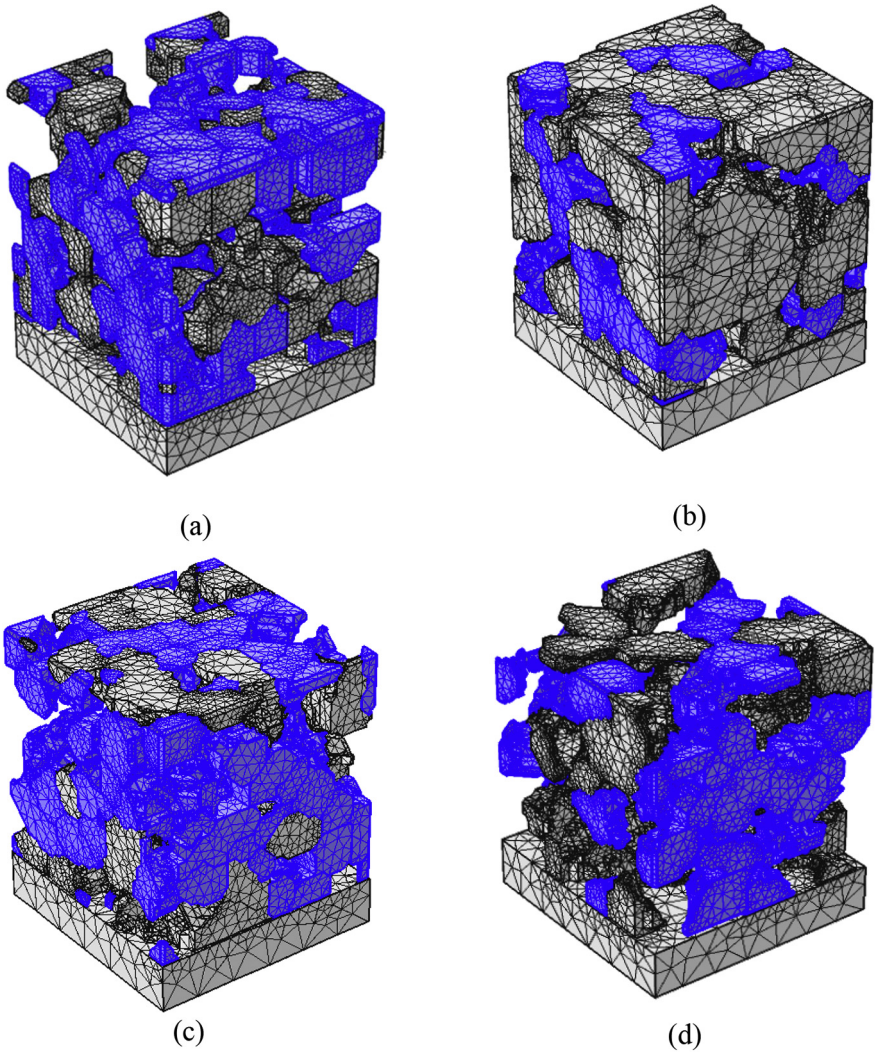

Fig. 2 – Different rate of species for Nickel/YSZ/Pore (blue: Nickel, gray: YSZ), (a) Standard distribution of the species (%35 Nickel, %30 YSZ and %35 Pore), (b) Increased rate of YSZ (%20 Nickel, %50 YSZ and %30 Pore), (c) Increased rate of Nickel (%50 Nickel, %20 YSZ and %30 Pore), (d) Increased rate of pores (%25 Nickel, %25 YSZ and %50 Pore). (For interpretation of the references to color in this figure legend, the reader is referred to the web version of this article.)

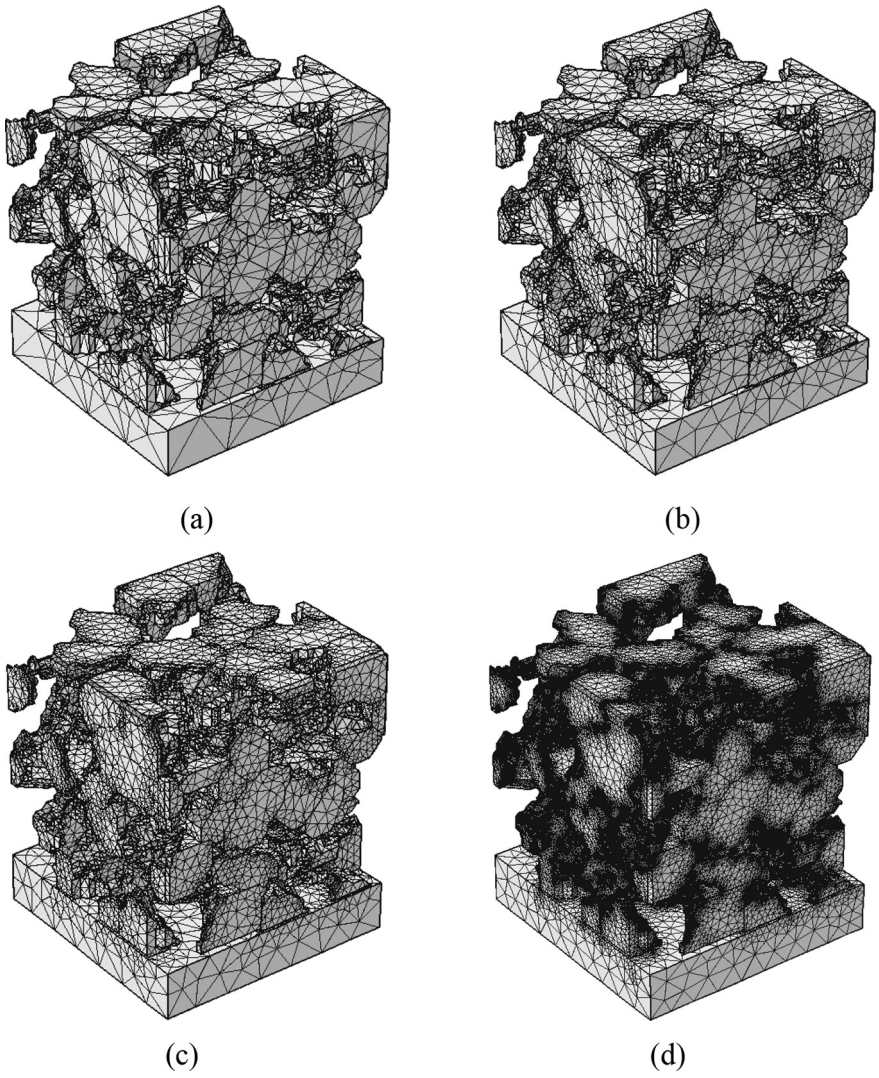

Fig. 3 – Comparison of the elements number (a) ~13.000 elements (b) ~80.000 elements (c) ~160.000 elements and (d) ~300.000 elements.

produce the best performance. The selected scenarios for the synthetic microstructures are given below and the generated microstructures are depicted in Fig. 2(a–d).

a. Standard composition (35% Nickel, 30% YSZ and 35% Pore)
b. Higher YSZ (20% Nickel, 50% YSZ and 30% Pore)
c. Higher Nickel (50% Nickel, 20% YSZ and 30% Pore)
d. Higher porosity (25% Nickel, 25% YSZ and 50% Pore)

Meshing process of the microstructures

In Dream 3D package, the meshing process of the created grains was carried out via surface meshing which is based on a multiple-material marching cubes algorithm [23]. The meshed grains were then saved in a binary stereo lithography (STL) file which describes each grain's surface mesh. However, these generated grains are not suitable for a direct analysis; therefore it is necessary to convert the grains in STL format to a solid structure in order to perform the thermal expansion analysis of cells in the Comsol software. Therefore, first, the generated and meshed grains using "*Dream 3D*" were classified phase by phase with "Paraview" software package [24] which allows the visualization of grains in STL format. Then the classified phase grains in the shell format were converted into

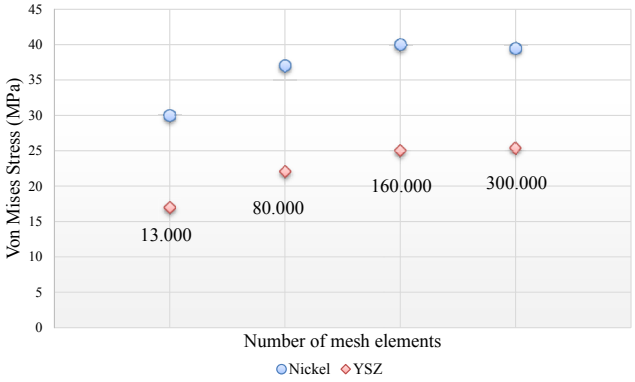

Fig. 4 – The change of mean stress with elements number.

Table 1 – Specifications of the elements.

Specifications	Values
Tetrahedral elements	160,014
Triangular elements	53,496
Edge elements	33,923
Vertex elements	16,074
Maximum elements size	0.191 μm
Minimum elements size	3.57E-2 μm
Maximum element growth rate	1.6
Curvature factor	0.7
Resolution of narrow regions	0.4

the solid grains. The converted phases were imported to Comsol in order to mesh as solid part with the tetragonal elements. The convergence of the finite element simulations is directly related to the number of elements and their types. Therefore the phases were meshed with different numbers of elements and the results were compared. Because of the complexity of the grains' surfaces, the tetragonal elements were used for each cases. The comparison of the element density only for the scenario "d" is given in Fig. 3. In Fig. 3(a–d), the numbers of elements are 13,000, 80,000, 160,000 and 300,000 in an order. The result of analysis of the element density is presented in Fig. 4 showing that the mean stresses do not change with increasing the number of elements after 160,000. Therefore, 160,000 elements were employed for all cases considered. The specifications of the elements are listed in Table 1. The numerical analyses were performed by Dell Precision™ T7500 work station which has 2 processor, 8 cores and 192 GB RAM.

Specifications of materials

Thermo-physical properties of the materials used in the analyses are given in Table 2 [25–28]. E is the elastic modulus (GPa) and α is the coefficient of thermal expansion (K^{-1}). The properties of material used in the numerical solution such as elasticity modulus and coefficient of thermal expansion are defined as functions of the temperature. These properties for Ni have already been defined in the software. For YSZ, on the other hand, the temperature dependent forms the modulus of elasticity and coefficient of thermal expansion of YSZ are

Table 2 – The properties of the materials used in the model [25–28].

Material	Nickel	8YSZ	NiO-8YSZ	Ni-8YSZ (reduced)
Temperature (K)	1073	1073	298	298
E (Gpa)	207	157	112.3	56.8
Poisson ratio (υ)	0.31	0.313	0.284	0.258
Specific heat capacity (J kg^{-1} K^{-1})	450	460	–	–
Density (kg/m^3)	8800	5200	–	–
Thermal conductivity (W m^{-1} K^{-1})	60.7	2.1	–	–
α (1.0×10^{-6})	13.5	10.5	12.5	12.5
Yield strength (MPa)	59	n/a	–	–
Tensile strength (MPa)	317	n/a	–	–

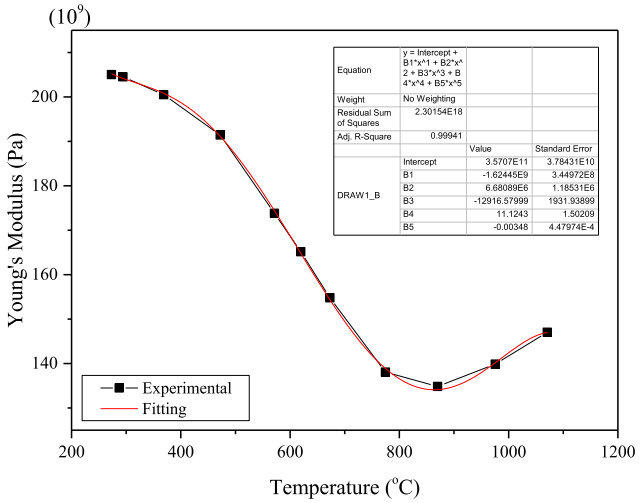

Fig. 5 – Young's Modulus of YSZ at different temperatures and curve fitting for YSZ [29].

obtained via curve fitting of the experimental data given Fig. 5 and Fig. 6 [29,30].

Governing equations

The displacement and stress generation due to thermal expansion mismatch are considered. Energy generation as a result of electrochemical reaction is neglected because of very small volume of computational domain chosen. The force balance for the solid body element in its differential form states:

$$\frac{\partial^2(\rho u)}{\partial t^2} - \nabla\cdot\sigma = \rho f \tag{1}$$

where u is the displacement vector, ρ is the density, f is the body force and σ is the stress tensor. The strain tensor ε, is defined in terms of u:

$$\varepsilon = \frac{1}{2}\left[\nabla u + (\nabla u)^T\right] \tag{2}$$

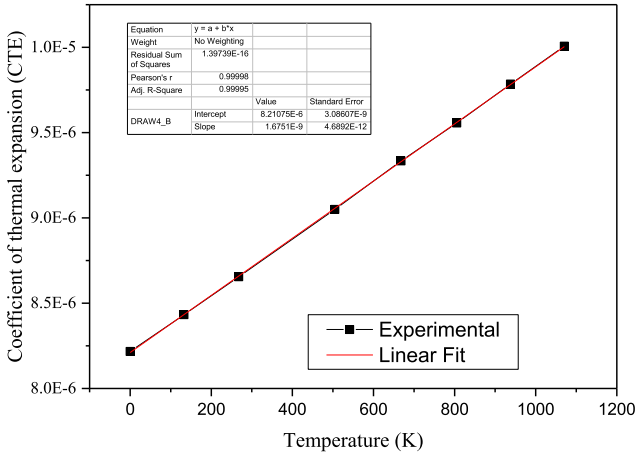

Fig. 6 – Coefficient of thermal expansion of YSZ at different temperatures and curve fitting for YSZ [30].

Table 3 – List of parametric studies.

Cases	Parameters	Microstructure	Temperature
Effect of temperature	700 °C 800 °C 900 °C	Standard composition	Variable
Effect of anode composition	Standard composition Higher YSZ Higher Nickel Higher porosity	Variable	800 °C
Effect of compression force	3 $kgcm^{-2}$ 5 $kgcm^{-2}$ 7 $kgcm^{-2}$ 9 $kgcm^{-2}$ 11 $kgcm^{-2}$	Higher porosity	800 °C

The Hooke's law, relating the stress and strain tensors, closes the system of equations:

$$\sigma = 2\mu\varepsilon + \lambda \mathrm{tr}(\varepsilon) I \tag{3}$$

where $\mathrm{tr}(\varepsilon)$ is the transpose of the strain tensor, I is the unit tensor and μ and λ Lame's coefficients, relating to Young's modulus of elasticity E and Poisson's ratio υ as:

$$\mu = \frac{E}{2(1+\upsilon)} \tag{4}$$

and

$$\lambda = \begin{cases} \dfrac{\upsilon E}{(1+\upsilon)(1-\upsilon)} & \text{for plane stress} \\ \dfrac{\upsilon E}{(1+\upsilon)(1-2\upsilon)} & \text{for plane strain and 3D} \end{cases} \tag{5}$$

There are well-known relationships between stress and displacement, and for plane stress with possible temperature loading these are [31]:

$$\sigma_{xx} = \frac{E}{(1-\mu^2)}\left\{\frac{\partial u}{\partial x} + \mu\frac{\partial v}{\partial y} - (1+\mu)\alpha T\right\} \tag{6}$$

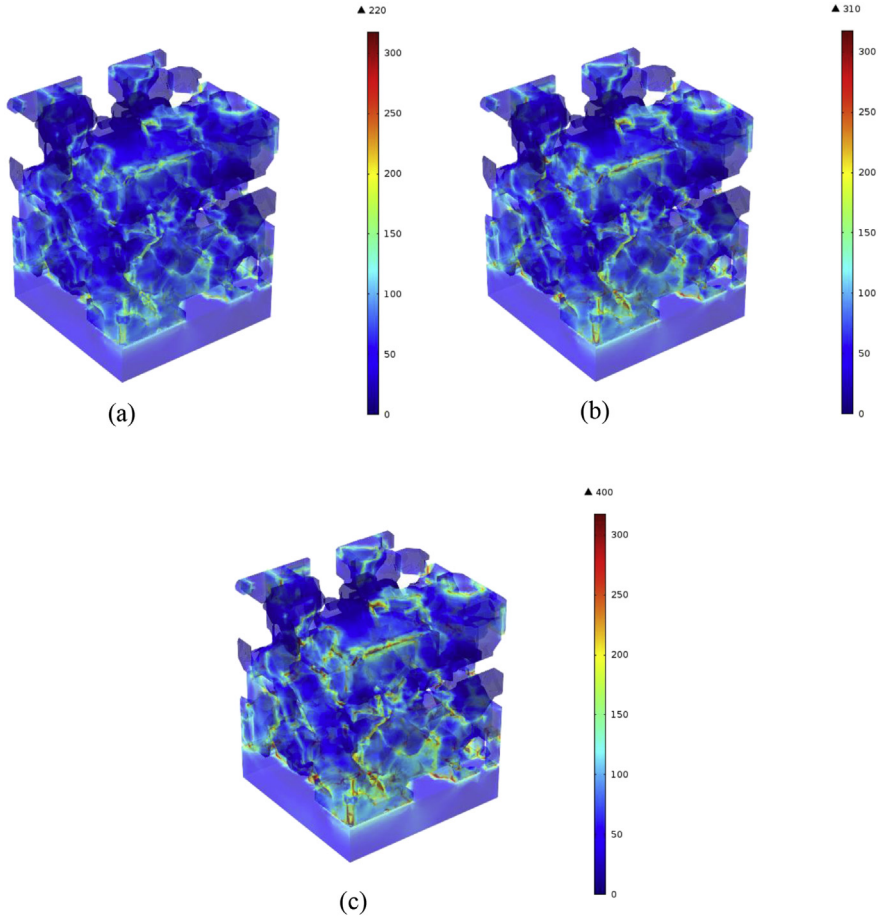

Fig. 7 – The stresses between Nickel/YSZ grains at different temperatures (Standard distribution-MPa), (a) 700 °C, (b) 800 °C and (c) 900 °C.

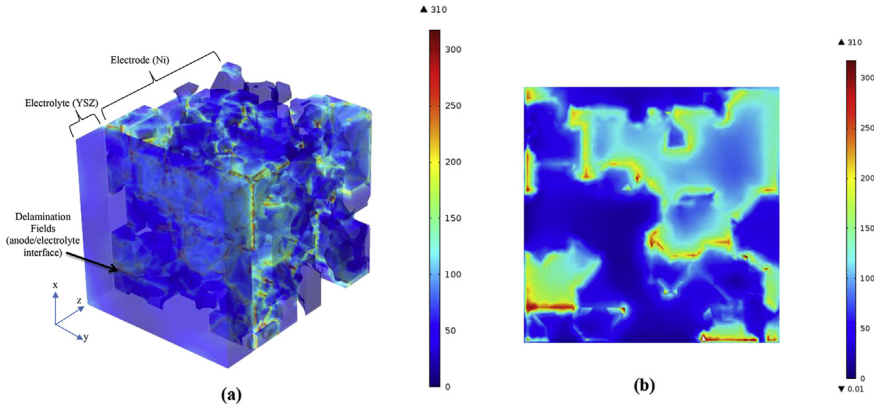

Fig. 8 – (a) The possible of delamination fields in the synthetic micro structure at 800 °C (Unit-MPa) (b) 2D stress distribution at the electrolyte/anode interface.

$$\sigma_{yy} = \frac{E}{(1-\mu^2)}\left\{\frac{\partial v}{\partial y} + \mu\frac{\partial u}{\partial yx} - (1+\mu)\alpha T\right\} \quad (7)$$

$$\sigma_{xy} = \frac{E}{2(1+\mu)}\left\{\frac{\partial u}{\partial y} + \frac{\partial v}{\partial x}\right\} \quad (8)$$

Using the above, the governing equation can be rewritten with the displacement vector u as the primitive variable [32]:

$$\frac{\partial^2(\rho u)}{\partial t^2} - \nabla\cdot\left[\mu\nabla u + (\nabla u)^T + \lambda I tr(\nabla u)\right] = \rho f \quad (9)$$

Boundary conditions

The solution of differential equations governing the stress distribution in the SOFC anode and electrolyte requires a careful identification of the boundary conditions. A temperature field of 25 °C was assumed as a zero stress condition like applied previously by Clague et al. [16], The temperature was subsequently increased to a temperature of 700 °C, 800 °C and 900 °C. In addition, the residual stresses which are likely to occur during the conversion of NiO to Ni are also neglected and the model is solved under steady state conditions.

The size of the generated cell was 10 μm × 10 μm × 10 μm and a symmetric condition was considered for the selected planes of the RVE except the bottom and upper surfaces in order to visualize the thermal expansions. The effects of applied force which is required to provide a contact between the interconnector and the cell were also studied. The contact force was varied between 3 kg cm^{-2} and 11 kg cm^{-2} in the numerical analyses. All considered cases are summarized in

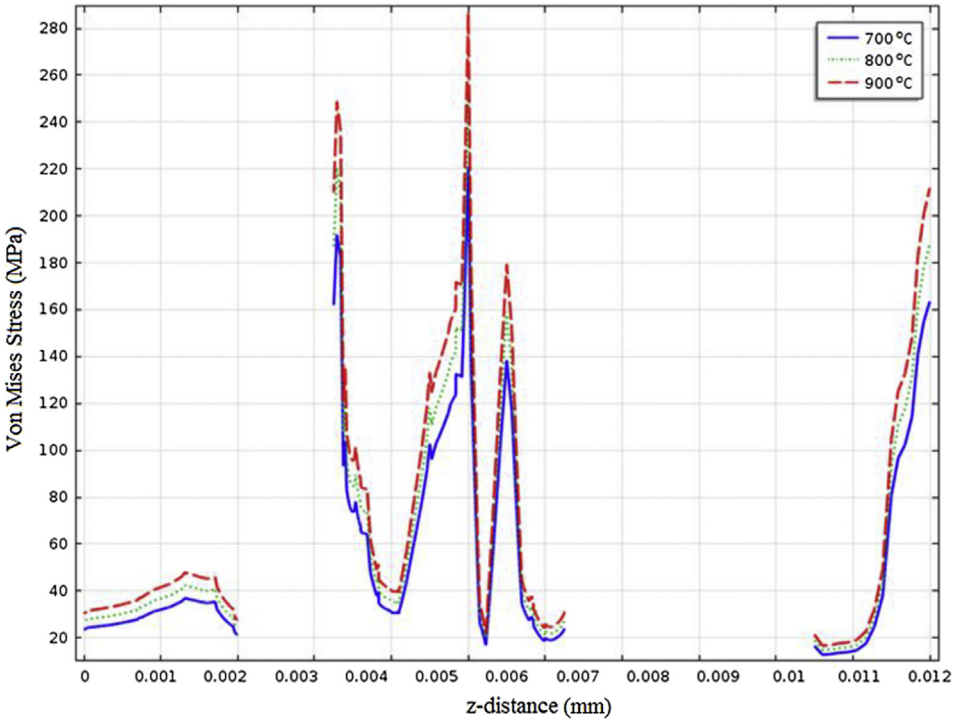

Fig. 9 – The stress distribution in the center of the cube along z direction at different temperatures.

Table 3. The selected symmetry planes for RVEs are depicted in Fig. 1. An isothermal situation was assumed in all cases considered due to a small portion of the cells investigated in all numerical studies. The thermal stresses occur only because of the different thermal expansion coefficient of the cell materials (eg. Ni, YSZ in this study).

Result and discussion

In the numerical studies, the effects of different amounts of anode electrode materials and porosity on the thermal stresses and the delamination features of anode electrode and grain interfaces are investigated.

Effects of temperature

Fig. 7(a–c) shows the maximum thermal stress fields calculated by changing the temperature from 25 °C to 700 °C, 800 °C and 900 °C. In Fig. 7(a), the maximum stress at 700 °C is about 220 MPa which is smaller than the failure strength of the materials. Fig. 7(b) depicts the thermal stresses at 800 °C which is the typical operating temperature of SOFCs. According to the simulation results, the maximum thermal stresses exceed the macroscopic tensile strength of 317 MPa at some intersections of Ni/YSZ grain boundaries. It means that the micro cracks due to the differences in the thermal expansions of the phases may be initiated at some Ni/YSZ interfaces. Fig. 7(c) shows that the maximum thermal stress increases to 400 MPa at 900 °C and it is seen that most of the anode is under high stresses. These results reveal that at high temperatures although the stresses do not exceed the maximum tensile stresses at whole anode, some Ni/YSZ interfaces can be expected to failure due the exceeding the yield stress. These findings also explain one of the reasons for the performance drop during SOFC operation. A partial performance loss usually observed during the SOFC operation is as result of some partial breakup of grain boundaries which blocks ion or electron transfer mechanism leading to the loss of triple phase boundaries.

Another commonly observed problem in SOFCs, which threats the integrity of the cell and causes a performance loss, is the delamination type damage which occurs between the interfaces of electrode and YSZ electrolyte during the operation due to the differences in the thermal expansion coefficients. Fig. 8 presents the stress levels calculated between the interfaces of electrode and YSZ electrolyte at 800 °C. 2D stress distribution at the electrolyte/anode interface is also

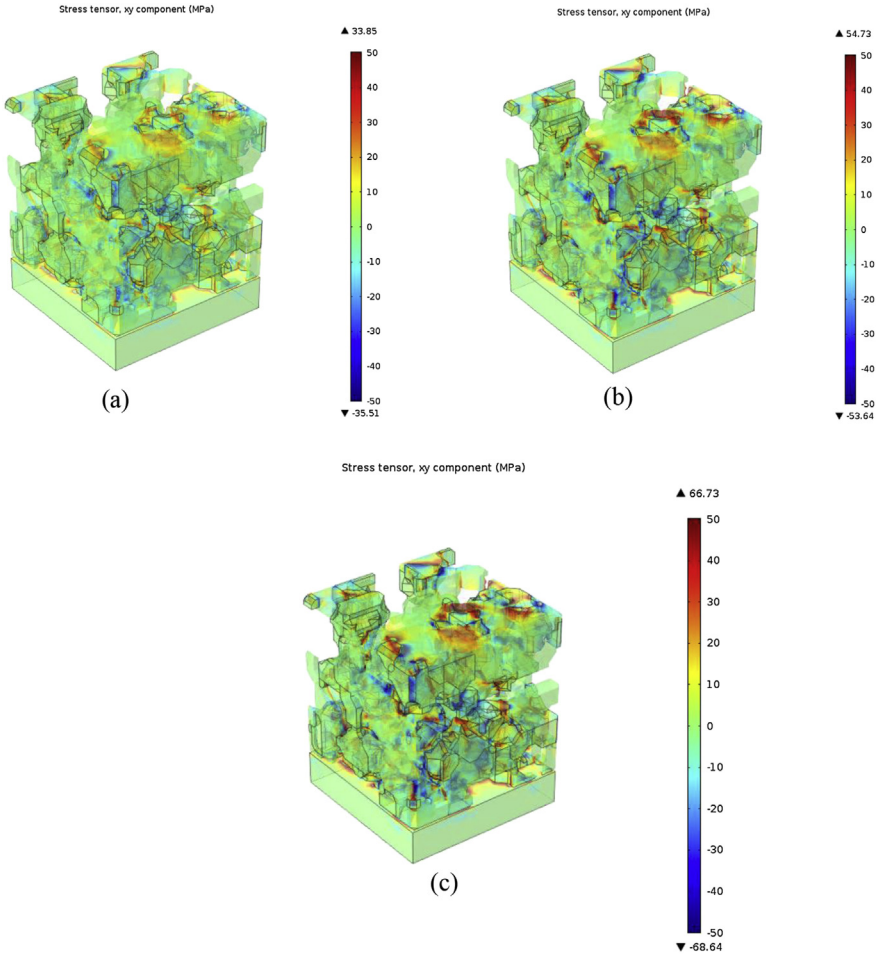

Fig. 10 – The shear stress at anode/electrolyte interface at different temperature in xy plane (a) 700 °C, (b) 800 °C and (c) 900 °C.

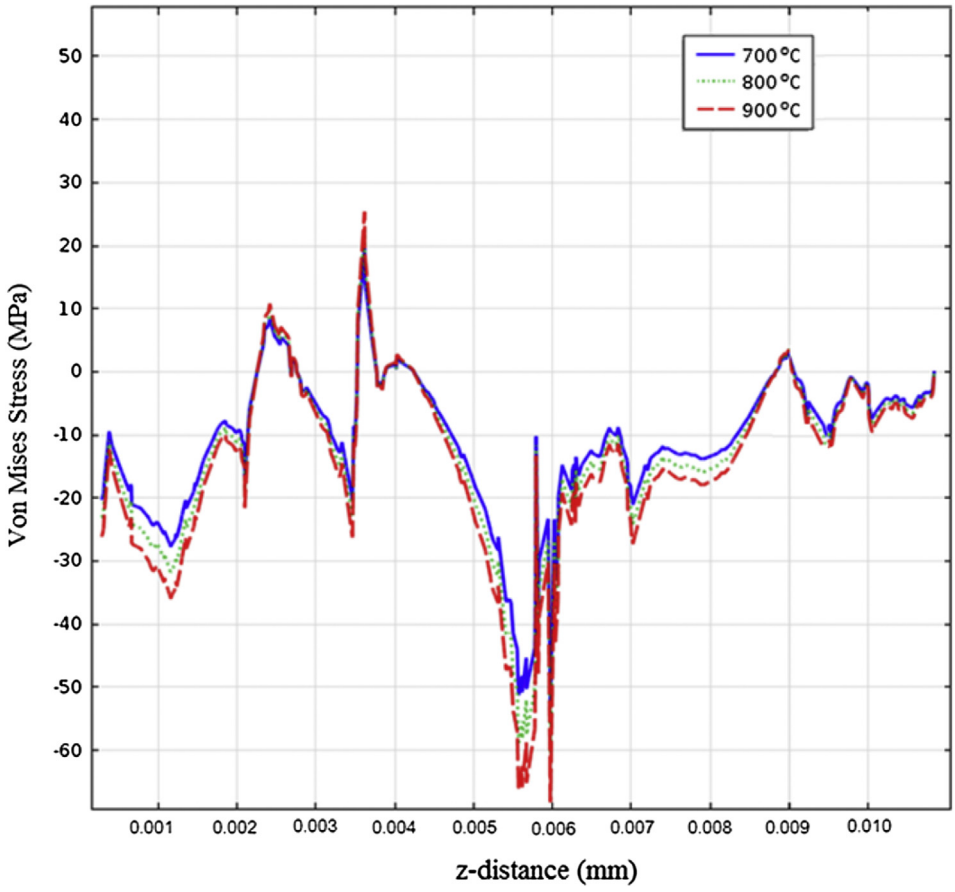

Fig. 11 – The graphical shear stress distribution at anode/electrolyte interface at different temperatures in *xy* plane.

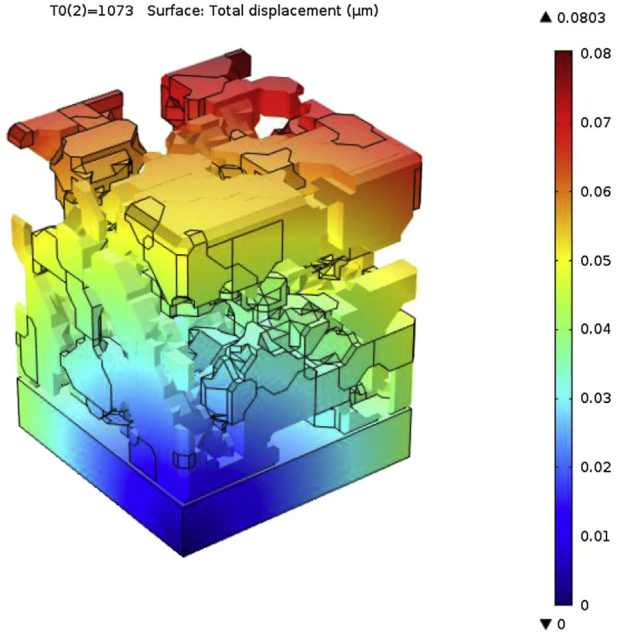

Fig. 12 – Total displacement of microstructure at 800 °C (mm).

included in the figure. The high stress areas can be evaluated as a potential region where the delamination can possibly occur. The stress concentration between the electrolyte and Ni interfaces is higher than those between the electrode and YSZ due to mainly the relatively higher thermal expansion coefficient of Ni.

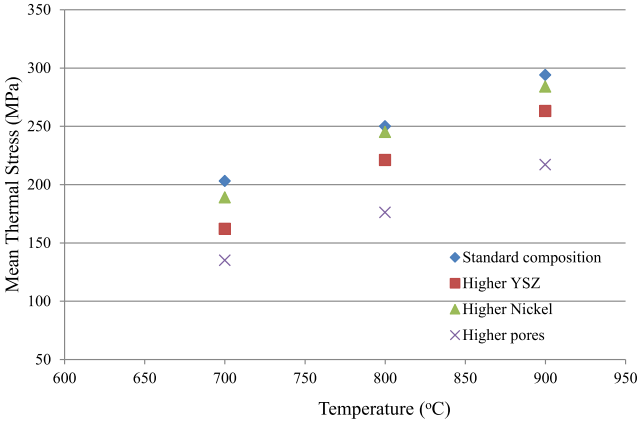

Fig. 13 – The mean stress distribution of grains in anode/electrolyte interface according to species distribution and temperature.

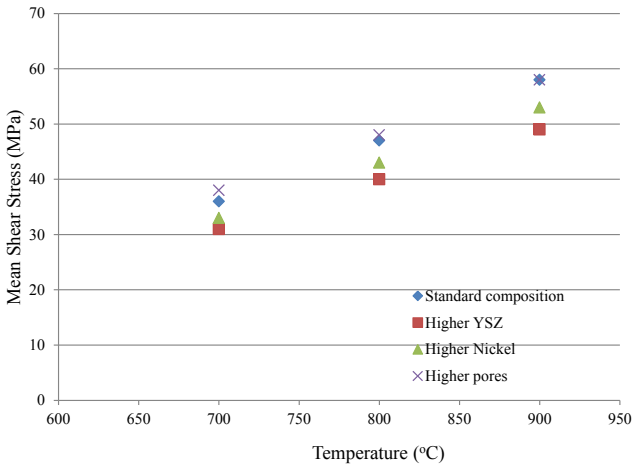

Fig. 14 – The mean shear stress distribution of grains in anode/electrolyte interface according to species distribution and temperature.

The stress concentrations along the z direction at the midpoint of the electrolyte are plotted in Fig. 9. In the figure, the blank regions correspond to the pores. It is seen that the stress increases with increasing the temperature in the selected direction. Zero thermal stress between 0.002 and 0.003 mm in z axis is calculated because of the available pores at that location.

Fig. 10(a–c) shows the maximum shear stress fields at 700 °C, 800 °C and 900 °C in an order. As given in Table 1, the shear stress should be less than 54 MPa for a safe operation. The shear stress is found not to exceed the material limits at 700 °C. However, the maximum shear stress (54 MPa) in the porous anode approaches the limit value when the temperature is increased to 800 °C (Fig. 10(b)) and exceeds the maximum value at 900 °C as seen in Fig. 10(c). The computed shear stress distribution on the xy plane of electrode/electrolyte interface is plotted in Fig. 11. It is seen that, the shear stress level increases with increasing the temperature in the selected direction. In

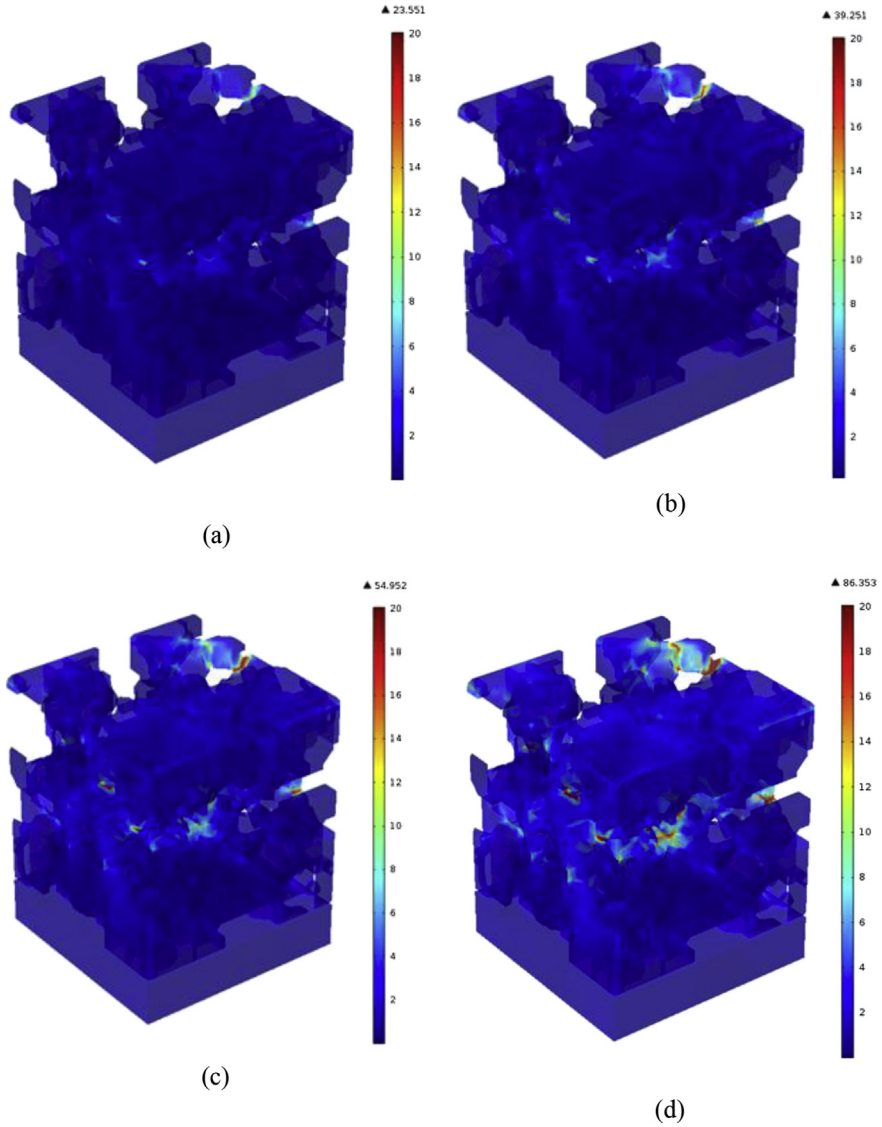

Fig. 15 – The effect of the contact pressure on the principal stress (Standard distribution, %35 Nickel, %30 YSZ and %35 Pore; 800 °C) (a) 3 kg cm^{-2} (b) 5 kg cm^{-2} (c) 7 kg cm^{-2} (d) 11 kg cm^{-2}.

addition, the shear stresses between the grains create compressive or tensile stress in the microstructure.

Fig. 12 shows the total displacement distribution in the z direction at 800 °C. It is seen that the upper part of the geometry having high nickel content shows a higher displacement. This can be attributed to the higher CTE of nickel compared to YSZ.

Effects of anode composition

The stress in the anode and anode/electrolyte interface is generated mainly because of the differences in the thermal expansion coefficients of the materials constituting the electrode and the electrolyte. Thus, altering the composition of the anode may affect the stress distribution. The effects of the anode composition on the stress distribution are presented in Fig. 13. It is seen that the stress increases with the temperature in all cases considered. On the other hands stress is found to decrease by increasing the YSZ or Ni content and the porosity of the anode. However, the anode porosity is show to be much more effective on the stress field. These results may be attributed to the stress relaxation through the pores which allows Ni or YSZ phase to expand without restriction releasing the stress. However, high porosity decreases overall electrode strength and the number of triple phase boundaries thus negatively affects the cell performance.

It is found that increasing the nickel content in the anode does not change the thermal stress significantly in spite of the relatively higher CTE of nickel. This result may be attributed to CTE mismatch which is the main stress mechanism in the anode structure. The amount of YSZ or Ni is almost doubled in each case considered thus CTE mismatch decreases.

Fig. 14 shows the shear stress on the *xy* plane of electrode/electrolyte interface for species distribution scenarios. The shear stress exceeds the limit only for 900 °C while it is in safe range for other operation temperatures (700–800 °C) studied.

Effects of compression force

The SOFC cell is usually compressed between the metallic interconnectors in the real operating conditions. The interconnectors provide pathways for the gas distribution and collect the electrical current produced in the cell. Since the anode of a cell is formed as a network of sintered grains with some porosity, uncontrolled compression force may break some or the entire solid network resulting in a serious performance loss. The problem alleviates when the compression force and thermally generated stress force are combined. Therefore, a parametric study is conducted to analyze the effect of compressive forces on the stress distribution in the anode microstructure. A range of compression forces between 3 kg cm^{-2} and 11 kg cm^{-2} is considered.

The results of the parametric study are presented in Figs. 15 and 16. The numerical results show that 5 kg cm^{-2} load creates 80 MPa additional stress in the microstructure. Further increase in the compressive load leads to stress values higher than the material limits. It is concluded that the fractured regions in the microstructure may increase due to the combined effects of the compressive force and the thermal stress. Therefore, the compressive force should be less than 5 kg cm^{-2} for a safe operation.

Conclusion

The thermo mechanical behavior of the porous anode and the electrode/electrolyte interface are numerically investigated at the microstructural level for various operating temperatures,

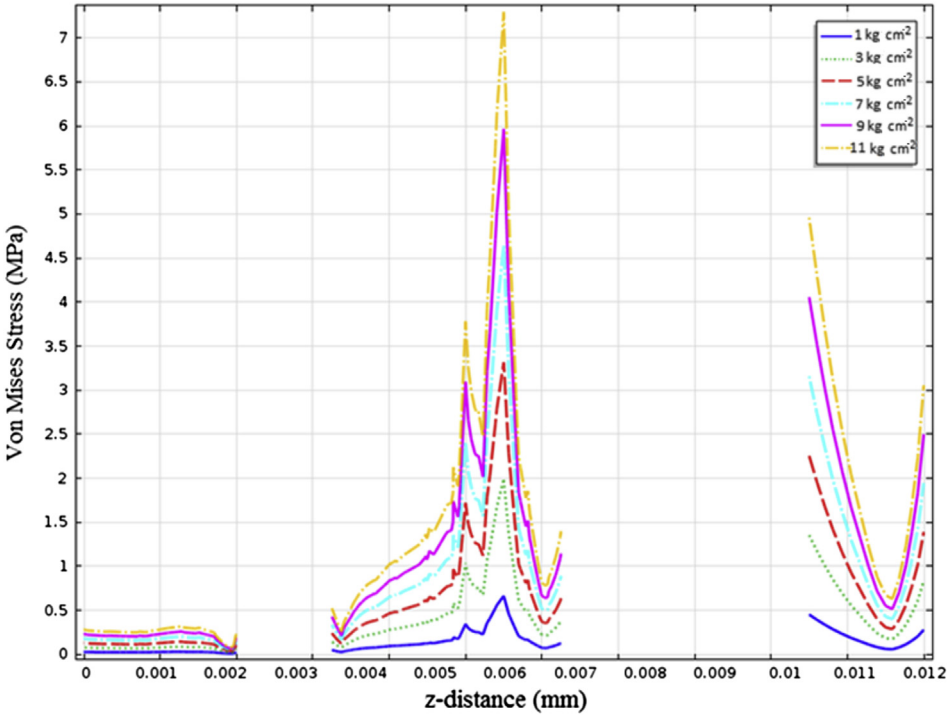

Fig. 16 – The effect of the contact pressure on the principal stress (graphical representation).

concentrations and compressive loads by a finite element analysis. The analysis is performed for understanding the deformation behavior of the anode microstructure due to the failure of the interfaces between phases constituting the anode microstructure under thermal stresses.

The anode microstructure composed of various Ni/YSZ and pores and the thermal stress distributions are obtained for various operation temperatures of 700, 800 and 900 °C. The numerical results show that the operation temperature of 800 °C is the critical one. At all operating temperature considered, the highest stresses are calculated at the electrode/electrolyte interface and Ni/YSZ grain interfaces in the electrode. The high stresses at these locations are considered as the reason for the delamination and micro cracks. The operating temperature has a significant effect on reducing the stresses at such interfaces. 800 °C is found to be highest allowable temperature for a safe operation of the systems considered in this study.

The effects of anode composition on the stress distribution as well as the porosity of the anode are also investigated. Increasing the nickel or YSZ content within the anode structure results in a lower stress, since increasing the amount of the same phase in the microstructure stabilizes the thermal expansion of the entire domain. The lowest stress values, on the other hand, are estimated at high porosities as expected. However, the cell performance may be adversely influenced by higher porosity because of the reduced number of electrochemically active sites.

The cell or the stacks is kept under compressive load in order to improve the current collection by improving the contact between metallic interconnect and the cell active area. Therefore, the magnitude of this force per unit area (cm^2) is also considered in this study. According to the simulation results, the applied load should be less than 5 kg cm^{-2}, in order to keep the stress level generated the microstructure within the material limits.

This study is for detailed understanding of the defects in the porous electrode structure as a result of the thermal expansion related to stresses and thus performance losses and the degradation of a solid oxide fuel cell. More accurate results may be obtained by considering the electrochemical reactions, fluid flow and species distributions which will be the subject of our ongoing study.

REFERENCES

[1] Singhal SC, Kendall K. High temperature solid oxide fuel cells. 1st ed. 2003. Genova.

[2] Celik S, Timurkutluk B, Mat MD. Measurement of the temperature distribution in a large solid oxide fuel cell short stack. Int J Hydrogen Energy 2013;38:10534–41.

[3] Fujita K, Somekawa T, Hatae T, Matsuzaki Y. Residual stress and redox cycling of segmented-in-series solid oxide fuel cells. J Power Sources 2011;196:9022–6.

[4] Somekawa T, Fujita K, Matsuzaki Y. Residual stress change with time of a segmented-in-series solid oxide fuel cell using an in situ X-ray stress measuring method. J Power Sources 2013;221:64–9.

[5] Doraswami U, Shearing P, Droushiotis N, Li K, Brandon NP, Kelsall GH. Modelling the effects of measured anode triple-phase boundary densities on the performance of micro-tubular hollow fiber SOFCs. Solid State Ionics 2011;192:494–500.

[6] Gostovic D, Smith JR, Kundinger DP, Jones KS, Wachsman ED. Three-dimensional reconstruction of porous LSCF cathodes. Electrochem Solid State Lett 2007;10:B214–7.

[7] Holzer L, Muench B, Wegmann M, Gasser P, Flatt RJ. FIB-nanotomography of particulate systems - part I: particle shape and topology of interfaces. J Am Ceram Soc 2006;89:2577–85.

[8] Holzer L, Munch B, Iwanschitz B, Cantoni M, Hocker T, Graule T. Quantitative relationships between composition, particle size, triple phase boundary length and surface area in nickel-cermet anodes for solid oxide fuel cells. J Power Sources 2011;196:7076–89.

[9] Kanno D, Shikazono N, Takagi N, Matsuzaki K, Kasagi N. Evaluation of SOFC anode polarization simulation using three-dimensional microstructures reconstructed by FIB tomography. Electrochim Acta 2011;56:4015–21.

[10] Shearing PR, Cai Q, Golbert JI, Yufit V, Adjiman CS, Brandon NP. Microstructural analysis of a solid oxide fuel cell anode using focused ion beam techniques coupled with electrochemical simulation. J Power Sources 2010;195:4804–10.

[11] Vivet N, Chupin S, Estrade E, Piquero T, Pommier PL, Rochais D, et al. 3D microstructural characterization of a solid oxide fuel cell anode reconstructed by focused ion beam tomography. J Power Sources 2011;196:7541–9.

[12] Vivet N, Chupin S, Estrade E, Richard A, Bonnamy S, Rochais D, et al. Effect of Ni content in SOFC Ni-YSZ cermets: a three-dimensional study by FIB-SEM tomography. J Power Sources 2011;196:9989–97.

[13] Wilson JR, Kobsiriphat W, Mendoza R, Chen HY, Hiller JM, Miller DJ, et al. Three-dimensional reconstruction of a solid-oxide fuel-cell anode. Nat Mater 2006;5:541–4.

[14] Shearing PR, Gelb J, Brandon NP. X-ray nano computerised tomography of SOFC electrodes using a focused ion beam sample-preparation technique. J Eur Ceram Soc 2010;30:1809–14.

[15] Grew KN, Peracchio AA, Chiu WKS. Characterization and analysis methods for the examination of the heterogeneous solid oxide fuel cell electrode microstructure: part 2. Quantitative measurement of the microstructure and contributions to transport losses. J Power Sources 2010;195:7943–58.

[16] Clague R, Shearing PR, Lee PD, Zhang Z, Brett DJL, Marquis AJ, et al. Stress analysis of solid oxide fuel cell anode microstructure reconstructed from focused ion beam tomography. J Power Sources 2011;196:9018–21.

[17] Gunda NSK, Choi HW, Berson A, Kenney B, Karan K, Pharoah JG, et al. Focused ion beam-scanning electron microscopy on solid-oxide fuel-cell electrode: image analysis and computing effective transport properties. J Power Sources 2011;196:3592–603.

[18] Carraro T, Joos J, Ruger B, Weber A, Ivers-Tiffee E. 3D finite element model for reconstructed mixed-conducting cathodes: I. Performance quantification. Electrochim Acta 2012;77:315–23.

[19] Digital representation environment for analyzing microstructure in 3D. 8 ed. 2013. http://dream3dbluequartznet.

[20] Groeber M, Ghosh S, Uchic MD, Dimiduk DM. A framework for automated analysis and simulation of 3D polycrystalline micro structures. Part 1: statistical characterization. Acta Mater 2008;56:1257–73.

[21] Groeber M, Ghosh S, Uchic MD, Dimiduk DM. A framework for automated analysis and simulation of 3D polycrystalline micro structures. Part 2: synthetic structure generation. Acta Mater 2008;56:1274–87.

[22] Tucker JC, Chan LH, Rohrer GS, Groeber MA, Rollett AD. Comparison of grain size distributions in a Ni-based superalloy in three and two dimensions using the Saltykov method. Scr Mater 2012;66:554–7.
[23] Wu Z, Sullivan JM. Multiple material marching cubes algorithm. Int J Numer Methods Eng 2003;58:189–207.
[24] ParaView - open source scientific visualization. 2013. www.paraview.org.
[25] Radovic M, Lara-Curzio E. Elastic properties of nickel-based anodes for solid oxide fuel cells as a function of the fraction of reduced NiO. J Am Ceram Soc 2004;87:2242–6.
[26] Atkinson A, Ramos TMGM. Chemically-induced stresses in ceramic oxygen ion-conducting membranes. Solid State Ionics 2000;129:259–69.
[27] Wang L, Wang Y, Zhang WQ, Sun XG, He JQ, Pan ZY, et al. Finite element simulation of stress distribution and development in 8YSZ and double-ceramic-layer La2Zr2O7/8YSZ thermal barrier coatings during thermal shock. Appl Surf Sci 2012;258:3540–51.
[28] Radovic M, Lara-Curzio E. Mechanical properties of tape cast nickel-based anode materials for solid oxide fuel cells before and after reduction in hydrogen. Acta Mater 2004;52:5747–56.
[29] Giraud S, Canel J. Young's modulus of some SOFCs materials as a function of temperature. J Eur Ceram Soc 2008;28:77–83.
[30] Vaidya S, Kim JH. Finite element thermal stress analysis of solid oxide fuel cell cathode microstructures. J Power Sources 2013;225:269–76.
[31] Fryer YD, Bailey C, Cross M, Lai CH. A control volume procedure for solving the elastic stress-strain equations on an unstructured mesh. Appl Math Model 1991;15:639–45.
[32] Jasak H, Weller HG. Application of the finite volume method and unstructured meshes to linear elasticity. Int J Numer Meth Eng 2000;48:267–87.